Ethylene Glycol Reforming on Pt(111): First-Principles Microkinetic Modeling in Vapor and Aqueous Phases

Muhammad Faheem[1,2], Mohammad Saleheen[1], Jianmin Lu[1,3], and Andreas Heyden[1,*]

[1]Department of Chemical Engineering, University of South Carolina, 301 South Main Street, Columbia, South Carolina 29208, United States

[2]Department of Chemical Engineering, University of Engineering & Technology, Lahore 54890, Pakistan

[3]State Key Laboratory of Catalysis, Dalian National Laboratory for Clean Energy, Dalian Institute of Chemical Physics, Chinese Academy of Sciences, Dalian 116023, Liaoning, China

*Corresponding author email: heyden@cec.sc.edu

ABSTRACT

First-principles, periodic density functional theory (DFT) calculations and mean-field microkinetic modeling have been used to investigate the decomposition of ethylene glycol for hydrogen production on Pt(111) in vapor and aqueous phases. All dehydrogenated species derived from ethylene glycol ($C_2H_xO_2$, x = 0–6) and methanol (CH_yO, y = 0–4), and all elementary C–C, C–H, and O–H bond breaking steps are included in the microkinetic model. Reaction path analysis in vapor phase indicates that both initial C–H and O–H dehydrogenation steps are kinetically relevant at all temperatures (470–530 K). Initial O–H bond cleavage is reversible at low temperatures but accounts for an increasingly dominant fraction of the total reaction flux at higher temperatures. C–C bond scission is observed only after significant dehydrogenation ($x \leq 3$) and is more likely to happen in surface intermediates where one of the cleavage products is CO. The process is highly selective to the production of H_2 compared to methanol. For aqueous-phase model development, free energies of solvation were computed for all surface intermediates and transition states using a continuum solvation approach. Our aqueous-phase microkinetic model predicts a 0.4 eV lower apparent activation energy and an order of magnitude larger turnover frequencies. Initial C–H bond cleavage becomes more important but the general trends are similar to the vapor phase, suggesting that the reaction chemistry is similar in both vapor and aqueous phases.

KEYWORDS

DFT; Ethylene glycol; Microkinetic modeling; Aqueous-phase reforming; Implicit solvation; Solvent effects

1. INTRODUCTION

The quest for alternative energy resources is driven by increasing global energy demands, rapidly depleting fossil fuel reserves, and environmental considerations. Utilization of lignocellulosic biomass as a renewable source of fuels and value-added chemicals has garnered significant interest in recent years and numerous chemical and catalytic strategies have been developed for biomass processing.[1-3] Biomass reforming for production of hydrogen (or syngas) is particularly attractive because the downstream technologies for conversion to liquid fuels and value-added chemicals are well-developed. Biomass-derived oxygenates are largely C_5- and C_6-sugars and their derivatives, and can be used for hydrogen production via aqueous-phase reforming (APR).[4-6] The process is typically carried out at elevated temperatures (200-250 °C) using supported metal catalysts with Pt showing highest activity and selectivity toward desired products.[7-8] Liquid phase is maintained by keeping the system pressure above the vapor pressure of water at the experimental temperature. Because of their high functionality, these oxygenated feeds are generally highly reactive and the conversion process is a complex reaction mechanism involving a myriad of reactions.[2] Understanding the mechanism and reaction pathways controlling these transformations is essential for rational catalyst design.

From a computational point of view, the number of possible elementary reactions and surface intermediates increases significantly with the size of the molecule of interest. Ethylene glycol (EG) is the simplest model molecule of various biomass-derived polyols that contains all relevant C–C, C–O, C–H, and O–H bonds and has a C:O stoichiometry of 1:1 with –OH groups on adjacent C atoms. Ethylene glycol decomposes according to the following reaction:

$$C_2H_6O_2 \rightarrow 2CO + 3H_2 \qquad \ldots(1)$$

This pathway implies cleavage of C–C, C–H, and O–H bonds. Water–gas shift (WGS) reaction is also favorable under typical APR conditions and CO produced by reaction (1) is largely removed as CO_2.[9-10]

$$CO + H_2O \rightleftharpoons CO_2 + H_2 \qquad \ldots(2)$$

Another possible pathway leads to formation of lower oxygenates and alkanes (for example, ethanol, acetaldehyde, and ethane) through C–O cleavage. Finally, CO and CO_2 can undergo hydrogenation to produce methanol.

Ethylene glycol reforming has been the subject of numerous experimental and computational studies.[10-16] Kandoi et al.[10] compared the kinetics of EG reforming over Pt in vapor and aqueous phases through microkinetic modeling based on a reduced mechanism of 7 lumped reactions. Brønsted–Evans–Polanyi-type correlations[17-18] developed for mono-functional alcohols[19-20] were used to estimate activation barriers for bond cleavage steps. Microkinetic model parameters were then fitted to the available experimental data.[11, 21] Salciccioli and coworkers[13-15] developed a detailed first-principles microkinetic model and successfully predicted intrinsic kinetic trends for Pt catalyzed vapor-phase EG decomposition. Christiansen and Vlachos[16] developed a similar model for Pt catalyzed vapor-phase steam reforming of EG by including water as a co-reactant. While these computational studies provide useful mechanistic insights, they fail to rigorously account for the influence of an aqueous environment on reaction kinetics and equilibria.

To address this lack of a fundamental understanding of the similarities and differences in the EG reforming chemistry in vapor and aqueous phases, we investigated in this study the mechanism of EG decomposition for hydrogen production on Pt(111) in both phases from first-principles calculations. First, we present a detailed vapor-phase microkinetic model similar to

Salciccioli and Vlachos[14] in order to establish a baseline for identification of most abundant surface intermediates, dominant reaction pathways, and general kinetic trends. Next, we reparametrize this model to account for the effect of an aqueous environment using a continuum solvation approach. Uncertainty in overall reaction mechanism and turnover frequency due to uncertainty in the cavity radii of transition metal elements in the continuum solvation approach has been carefully studied. The microkinetic model does not include any adjustable parameter to fit experimental data and no a priori assumption is made about the relative importance of surface intermediates or elementary reactions. Model predicted apparent activation energy, reaction orders, and sensitivity coefficients are compared between vapor and aqueous phases revealing general trends in broad agreement with previous experimental and computational studies. We close with a remark on inclusion of dispersion effects for improving agreement with experimental data.

2. COMPUTATIONAL METHODS

2.1. Periodic Planewave DFT Calculations

Periodic DFT calculations were performed using the Vienna *Ab Initio* Simulation Package (VASP 5.2).[22] A planewave basis set with a cutoff energy of 400 eV was used to solve the Kohn–Sham equations. Ionic core potentials were described using the projector augmented wave (PAW) method.[23] Electron exchange and correlation effects were included within the generalized gradient approximation (GGA) using the functional proposed by Perdew, Burke, and Ernzerhof (PBE).[24-25] Fractional occupancies of bands were allowed within a window of 0.10 eV using a first-order Methfessel–Paxton smearing method.[26] All self-consistent field (SCF) calculations were converged to 1.0×10^{-7} eV. The total energy of fcc-Pt bulk was minimized using a 17 × 17 × 17

Monkhorst–Pack k-mesh.[27] The calculated equilibrium lattice constant (3.976 Å) is in reasonable agreement with the experimental value (3.92 Å).

Using the supercell approach, Pt(111) surface was constructed as a large 4 × 4 unit cell with four layers of Pt atoms and a vacuum of 15 Å to minimize interaction between periodically repeated images. For all slab calculations, the bottom two Pt layers were fixed at their bulk positions. A 4 × 4 × 1 Monkhorst–Pack k-mesh was employed for sampling the Brillouin zone. Dipole and quadrupole corrections to the energy were included using a modified Makov–Payne method.[28] Harris–Foulkes-type corrections for forces were taken into account. Geometry optimizations were stopped when the force on each relaxed atom was smaller than 0.02 eV/Å. A two-step procedure was adopted for all transition state searches. First, an approximate reaction coordinate between the reactant and product states was constructed as a series of intermediate images. After optimizing this chain with the climbing-image nudged elastic band method,[29] the image closest to the likely transition state was used as an initial guess for the dimer method.[30-31] All minima and transition state structures were confirmed through dynamical matrix calculations based on numerical second derivatives of the energy.

2.2. Implicit Solvation (iSMS)

In this study, the influence of an aqueous environment on reaction kinetics and equilibria is explored using our recently developed *iSMS* method.[32] The principal idea of this approach is to account for the long-range metal interactions within the framework of DFT calculations using a periodic slab model in the absence of solvent, and to include the effect of solvent as a localized perturbation of free energy differences that can be described using a cluster model embedded in an implicit solvent. The free energy of an adsorbed intermediate on a “periodic” metal slab in solvent, $G^{\text{liquid}}_{\text{surface+adsorbate}}$, is then obtained using a simple subtraction scheme

$$G^{\text{liquid}}_{\text{surface+adsorbate}} = E^{\text{vacuum}}_{\text{surface+adsorbate}} + G^{\text{liquid}}_{\text{cluster+adsorbate}} - E^{\text{vacuum}}_{\text{cluster+adsorbate}} \qquad \ldots(3)$$

where $E^{\text{vacuum}}_{\text{surface+adsorbate}}$ is the planewave DFT energy for the periodic slab in vacuum, $G^{\text{liquid}}_{\text{cluster+adsorbate}}$ is the free energy in solvent (without explicitly including vibrational contributions) for a metal cluster constructed by removing selected metal atoms from the periodic slab model and removing the periodic boundary conditions, and $E^{\text{vacuum}}_{\text{cluster+adsorbate}}$ is the DFT energy of the same cluster in the absence of solvent. Convergence properties of iSMS with respect to the size of the metal cluster and the basis set have previously been published.[32] In this study, we have used a two-layer, 51-atom, Pt(111) cluster to calculate the free energies of solvation for all surface intermediates and transition states. Vibrational contributions to the free energy were included using gas-phase frequencies obtained from periodic slab calculations assuming that the structure of an adsorbed moiety does not change significantly in solvent.[33-34]

The TURBOMOLE 6.4[35-36] program package was used for nonperiodic cluster calculations. All-electron basis sets of triple-ζ quality were used for adsorbate atoms (C, O, and H).[37] Relativistic small-core effective core potentials (ECPs) were used for Pt atoms and only their valence electrons were represented using triple-ζ quality basis sets.[38] Electron exchange and correlation effects were accounted for using the B-P86 functional[39-40] as required by the parametrization of the implicit solvation model used in this study. The RI-J approximation with auxiliary basis sets was used to approximate Coulomb potentials.[41] For all nonperiodic structures, multiple spin states were tested using an SCF convergence criterion of 1.0×10^{-7} hartree and spherical grid m4.[42] Only for the lowest-energy spin state, COSMO[43-44] calculations were performed using radii-based cavities and a dielectric constant of infinity. For these calculations, SCF convergence criterion and spherical grid were changed to 1.0×10^{-8} hartree and m5, respectively. Free energies of solvation were computed using COSMO-RS.[45] Thermodynamic properties of water (solvent) were obtained from the COSMOtherm database,[46] based on parametrization of the results of quantum chemical COSMO calculations at the BP-TZVP level of theory. We note that implicit solvation models have inherent challenges in properly describing hydrogen bonding; however, COSMO-RS includes a parameterized hydrogen bonding energy based on the screening charge densities of the hydrogen bond acceptor and donor.[46]

3. MODEL DEVELOPMENT

3.1. Microkinetic Modeling

A mean-field microkinetic model was developed for reaction pathway analysis under realistic process conditions. All dehydrogenated species derived from ethylene glycol ($C_2H_xO_2$, x = 0–6) and methanol (CH_yO, y = 0–4), and all elementary C–C, C–H, and O–H bond breaking steps were included. We note here that C–O bond scission in EG leads to formation of ethanol and ultimately ethane. However, experimental studies of EG reforming over Pt have shown only trace amounts of these products.[10, 21] We confirmed this overall conclusion by computing activation barriers for C–O cleavage in selected surface intermediates. These barriers were found to be significantly higher than the barriers for C–C cleavage in the same intermediates. For these reasons, C–O bond scissions were not included in the microkinetic model. In addition, considering the low levels of CO reported in the product stream,[9-10] we assume that the WGS reaction approaches equilibrium at all temperatures and the CO concentration in the effluent stream is 500 ppm. Elementary reactions pertaining to the WGS mechanism are not explicitly considered.

All reactions were assumed to be reversible. The net rate of a reaction i is given by

$$r_i = k_{f,i} \prod_{j=1,n_j<0}^{j=N} C_j^{-n_j} - k_{r,i} \prod_{j=1,n_j>0}^{j=N} C_j^{n_j} \qquad \ldots(4)$$

where $k_{f,i}$ and $k_{r,i}$ are the forward and reverse reaction rate constants, respectively. Index j loops over all N species involved in the reaction, and the corresponding concentration C_j equals either a fractional surface coverage $\left(\theta_j\right)$ or a gas-phase partial pressure $\left(P_j\right)$. The stoichiometric coefficient n_j is negative for reactants and positive for products. For all surface reactions, forward rate constants were calculated using harmonic transition state theory.[47]

$$k_{f,i} = \frac{\gamma k_B T}{h} \exp\left(\frac{-\Delta G_i^{\ddagger}}{k_B T}\right) \qquad \ldots(5)$$

Here, $\Delta G_i^{\ddagger}$ is the free energy of activation, T is the absolute temperature, and k_B and h are respectively the Boltzmann and Planck constants. The transmission coefficient γ was assumed to be 1.0 for all cases. Zero-point energies and (harmonic) vibrational partition functions were calculated using vibrational frequencies $\left(\nu_i\right)$ derived from planewave DFT calculations.

$$E_{zpv} = \sum_i \frac{h\nu_i}{2}; \qquad q_{vib} = \prod_i \left[1 - \exp\left(\frac{-h\nu_i}{k_B T}\right)\right]^{-1} \qquad \ldots(6)$$

We note here that the top two Pt layers were relaxed during geometry optimization but fixed for frequency calculations. This procedure reduces the accuracy of low-frequency modes that are coupled with the metal atoms. Considering that the harmonic approximation is least accurate for small wavenumbers, we shifted all (real) frequencies for adsorbed intermediates and transition states below 100 cm^{-1} to 100 cm^{-1}. These low-frequency modes thus cancel out for surface reactions and have no effect on reaction free energies and activation barriers. This adjustment is not required for gas-phase molecules because the translational and rotational degrees of freedom are projected out and the respective partition functions are rigorously included using statistical mechanics.[48]

Adsorption was assumed to be a nonactivated process and collision theory was used to calculate the forward rate constants.

$$k_{f,i} = \frac{S\sigma}{N\sqrt{2\pi M_i k_B T}} \qquad \ldots(7)$$

Here, N/S is the number of catalytic sites per unit surface area and M_i is the molecular weight of the adsorbate. The sticking probability σ was assumed to be 1.0 for all cases. Equation (7) thus gives an upper limit for the adsorption rate constant. As we will show later, the rates of adsorption–desorption processes are many orders of magnitude faster than the rates of surface reactions and these processes may be assumed to be in equilibrium. To ensure thermodynamic consistency, reverse rate constants were always calculated from the thermodynamic equilibrium constants $\left(K_{eq}\right)$.

$$K_{eq,i} = \exp\left(\frac{-\Delta G_i}{k_B T}\right); \qquad k_{r,i} = \frac{k_{f,i}}{K_{eq,i}} \qquad \ldots(8)$$

where ΔG_i is the Gibbs free energy of reaction.

With all rate parameters known, a microkinetic model was developed as a system of ordinary differential equations. At steady state, the fractional coverage of a surface intermediate is given by

$$\frac{d\theta_j}{dt} = \sum_i \nu_{j,i} r_i = 0 \qquad \ldots(9)$$

where index i loops over all reactions. In addition, the total number of sites is conserved.

$$\sum_j n_j \theta_j = 1 \qquad \ldots(10)$$

A complete list of the number of sites assigned to each species $\left(n_j\right)$ is provided in the Supplementary Information. All microkinetic simulations were initialized with a clean Pt surface and solved as a system of differential algebraic equations using the BzzMath library[49] to obtain steady state fractional surface coverages and turnover frequencies (TOFs). Although significantly slower than a nonlinear solver,[50] this approach offers higher numerical stability and is essentially independent of the initial guess.

3.2. *Adsorbate–Adsorbate Lateral Interactions*

It is well known that at high CO coverage on Pt(111), adsorbed CO molecules destabilize the binding strength of each other resulting in a decrease of the adsorption energy.[51-52] Preliminary results of a vapor-phase microkinetic model showed that if these lateral interactions are not considered, the surface is completely poisoned by CO. That is, adsorbate–adsorbate interactions must be included in the microkinetic model to better describe the state and condition of the catalytic surface in a realistic reaction environment. In order to obtain coverage dependent adsorption energies of CO and H, DFT calculations were performed at various surface coverages on a 3 × 3 × 4 Pt(111) slab. Possible permutations of co-adsorbed species were taken into account and all such configurations were Boltzmann-averaged at 500 K. More information about this data set is provided in the Supplementary Information. For CO–CO, H–H, and CO–H lateral interactions, we used the functional form proposed by Grabow et al.[52] For all other surface intermediates and transition states, destabilization due to CO and H was assumed to be similar[14] and the corresponding parameters were derived from DFT calculations with co-adsorbed EG. Finally, destabilization of surface intermediates due to interactions among them was described by the same parameters as used for CO–CO interaction. We note here that the value of this parameter is not significant since the coverage of these species is very small compared to CO and H. A summary of all adsorbate–adsorbate interaction parameters is shown in Table 1.

4. RESULTS AND DISCUSSION

4.1. Vapor Phase Dehydrogenation of $C_2H_xO_2$ and CH_yO Species

Energetics of all dehydrogenated species derived from ethylene glycol ($C_2H_xO_2$, x = 0–6) and methanol (CH_yO, y = 0–4) have been systematically investigated in this study. Binding modes for the most stable adsorption geometries of all intermediates are provided in the Supplementary Information. Reaction energies and activation barriers for all surface reactions are listed in Table 2. Adsorption energies are listed in Table 3.

Ethylene glycol binds to the Pt(111) surface through one of the –OH groups which points to the other –OH group forming an intramolecular hydrogen bond. This adsorption geometry is different from the one reported by Salciccioli et al.[53] who found that both oxygen atoms bind to adjacent top sites of Pt. The calculated adsorption energies are however in good agreement (−0.46 eV calculated in this work versus −0.49 eV previously reported). Both carbon atoms are far from the surface and must overcome steric hindrance of the –OH groups and H atoms to allow for C–Pt interaction. As a result, the barrier for C–C cleavage in EG is very high (2.07 eV) and initial dehydrogenation of EG is necessary.

Two possibilities exist for initial dehydrogenation of EG on Pt(111). DFT calculations predict that initial C–H bond scission is thermodynamically favored $\left(\Delta E_{rxn} = -0.48\,\mathrm{eV}\right)$ over initial O–H bond scission $\left(\Delta E_{rxn} = +0.40\,\mathrm{eV}\right)$. However, in the most stable adsorption configuration, the H atom from the –OH group is already in close proximity to the surface, whereas an α-H atom can come close to the surface only after significant rotation of the $–CH_2OH$ group.

As a result, the transition state for initial O–H scission is predicted to be 0.12 eV lower than that for initial C–H scission. This difference in activation barriers is small and we can expect both pathways to be competitive.

Thermodynamic analysis of all subsequent dehydrogenation steps reveals a similar trend. C–H bond scission is always exothermic and thermodynamically favored over O–H bond scission in the same surface moiety. After initial dehydrogenation, EG-derived species bind strongly to the surface in a manner that unsaturated C atoms satisfy their tetrahedral bonding geometry. Unsaturated O atoms, if present, bind to the surface to complete a total of two bonds. The only exception is the aldehyde (–CHO) group which can leave the surface and bind through an O atom (for example, in COH-CHO). Among equally dehydrogenated intermediates, species that bind through a C atom (–CHOH group) are more stable than the species that bind through an O atom (–CH_2O group). Formation of an intramolecular hydrogen bond (for example, in CHOH-CHOH) is energetically favorable. Deeper dehydrogenation results in stronger adsorption and lower barrier for C–C cleavage reactions. Previous computational studies have reported similar observations.[13, 53]

There are two possible $C_2H_5O_2$ intermediates. After initial C–H scission, the barrier for α-H abstraction in CHOH-CH_2OH to COH-CH_2OH (0.37 eV) is similar to that for β-H abstraction to CHOH-CHOH (0.35 eV), although the latter is slightly thermodynamically favored. After initial O–H scission, abstraction of α-H in CH_2O-CH_2OH to CHO-CH_2OH (glycolaldehyde) requires a very small barrier of 0.11 eV compared to 0.34 eV for abstraction of β-H to CH_2O-CHOH. Cleavage of O–H bonds in either $C_2H_5O_2$ species is highly unfavorable compared to C–H bond scission.

There are five possible $C_2H_4O_2$ intermediates. The lowest activation barrier (0.05 eV) at this level of dehydrogenation is observed for decomposition of CH_2O-CHOH to CHO-CHOH (from the initial O–H bond scission pathway). Decomposition of glycolaldehyde on the same pathway requires a considerably higher activation energy (0.37 eV). For the initial C–H bond scission pathway, the lowest barrier (0.20 eV) is observed for O–H bond cleavage in COH-CH_2OH to produce CO-CH_2OH. This is the first species in this reaction mechanism where the barrier for C–C cleavage is low enough to be competitive with the dehydrogenation reactions. In addition, the pathways through initial C–H and O–H bond scissions start to merge at this level of dehydrogenation.

Among the five possible $C_2H_3O_2$ intermediates, the most plausible dehydrogenation steps are C–H bond scission in CHO-CHOH (barrier = 0.27 eV) and O–H bond scission in COH-CHOH (barrier = 0.41 eV), both leading to the same product, CO-CHOH. Decomposition of CO-CH_2OH to CO-CH_2O has a comparable barrier (0.45 eV). This is followed by a small barrier (0.16 eV) for decomposition to CO-CHO. Removal of the last H atom from CO-CHO has almost the same barrier as C–C bond cleavage in this intermediate, with the latter being the thermodynamically preferred pathway by about 0.6 eV. C–C bond cleavage in completely dehydrogenated CO-CO occurs without an activation barrier.

Methanol also binds to the Pt(111) surface through the –OH group. The calculated adsorption energy of −0.27 eV is comparable to the previously reported value of −0.33 eV.[54] While the –CH_3 group is initially far from the surface, unlike ethylene glycol, there is no steric hindrance and α-H atoms can easily come close to the metal. As a result, the barriers for C–H cleavage are smaller than the barriers for O–H cleavage in all methanol-derived surface intermediates. As before, species that bind through carbon are energetically more stable than the species that bind through oxygen.

4.2. Vapor-Phase Microkinetic Model

A detailed vapor-phase microkinetic model was developed to establish a baseline for identification of the most abundant surface intermediates, dominant reaction pathways, and general kinetic trends. The feed stream consisted of 10 mole percent EG at a total pressure of 1 bar. Conversion of EG was assumed to be 1% to simulate the differential reactor operation. The WGS reaction was assumed to be in equilibrium and the CO concentration in the effluent stream was held fixed at 500 ppm. In the overall reforming reaction, 1 mole of EG is converted to 5 moles of H_2. All turnover frequencies (TOFs) reported in this work are based on a rate of EG consumption per second and should be multiplied by 300 for comparison with the experimental data of Kandoi et al.[10] (which are reported based on a H_2 production rate per minute).

Reference simulations for the determination of the most abundant surface intermediates were performed over a temperature range of 470 K to 530 K (Figure 1). CO* and H* are the most abundant adsorbates over this entire temperature range. The coverage of CO* is 41% at 470 K and only slightly decreases to 38% at 530 K. The coverage of H* is more sensitive to temperature and decreases from 45% at 470 K to 35% at 530 K. A small coverage of COH* (≈ 0.6%) is observed at lower temperatures but quickly disappears as the temperature is increased. Coverage of all other adsorbates is negligible. The predicted turnover rates are generally an order of magnitude smaller than the experimental data.[10] Given the uncertainty associated with DFT-predicted binding energies, the possibility of more active catalytic sites (for example, edges and corners), and a rudimentary description of adsorbate–adsorbate interactions, this level of disagreement between model-predicted and experimental TOFs is acceptable.

Table 4 shows a comparison of the model-predicted apparent activation energy and reaction orders with previously reported data. Both CO and H have a poisoning effect on the catalyst as evidenced by negative reaction orders of –0.58 and –0.84, respectively. For these simulations, the CO or H_2 gases were co-fed at concentrations indicated in Figure 2A and B, respectively. An increase in EG pressure has a positive effect on the overall TOF (Figure 2C). The predicted reaction order (1.0) however differs from the observed fractional order (0.4). The DFT-predicted equilibrium constant for EG adsorption is very small compared to the equilibrium constants for CO adsorption and H_2 dissociation. As a result, the coverage of $C_2H_xO_2$ intermediates is much smaller than the available free sites at all temperatures and increases proportionally with increase in EG partial pressure without significantly decreasing the availability of free sites; thus, leading to an apparent first order effect on the overall TOF. For the same reason, the predicted apparent activation energy is higher than the reported values. As we will show later, initial steps in this mechanism are rate limiting. Therefore, the apparent activation energy is strongly correlated to the energy of these transition states relative to gas-phase ethylene glycol. A large positive free energy of EG adsorption (Table 3) shifts these transition states upwards on a free energy scale (Figure 3) resulting in a higher overall activation energy. In section 4.4, we discuss a possible solution to this problem by inclusion of dispersion effects on adsorption energies.

The inhibiting effect of total pressure is correctly predicted (Figure 2D). These simulations were performed by varying the total pressure while maintaining the fixed feed composition and conversion of 1%. While an increase in EG partial pressure increases the reaction rate, site blocking due to increased partial pressures of CO and H becomes more significant, resulting in an overall negative reaction order (–0.13) with respect to the total pressure. Figure 2D shows that this effect is even more pronounced at higher total pressures (reaction order changes to –0.7).

An analysis of steady state reaction fluxes can provide useful insights into the reaction mechanism and dominant pathways under realistic reaction environments. Figure 3 shows the fraction of the overall reaction flux passing through various pathways in vapor-phase EG reforming at 500 K. The dominant mechanism for EG decomposition is through initial O–H bond cleavage which is in agreement with TPD experiments.[13] While initial C–H bond scission is irreversible, the relatively small reverse barrier for initial O–H bond scission causes this reaction to have a considerable rate in both directions. Altogether, both initial C–H and O–H bond scission pathways contribute significantly to the overall rate of EG decomposition. Partial equilibrium (PE) analysis[55] indicates that the reversibility of the initial O–H bond breaking reaction decreases at higher temperatures. The PE ratio (ϕ_i) is defined as the ratio of the forward reaction rate to the sum of forward $(r_{f,i})$ and reverse $(r_{r,i})$ reaction rates.

$$\phi_i = \frac{|r_{f,i}|}{|r_{f,i}| + |r_{r,i}|} \qquad \ldots(11)$$

A PE ratio is 1.0 for an irreversible reaction in the forward direction and 0.5 for a reaction where the forward and reverse reaction rates are equal. Initial C–H bond scission has a PE ratio of 1.0 over the temperature range explored in this study. In contrast, at lower temperatures the PE ratio for the initial O–H bond cleavage reaction is only slightly larger than 0.5 (computed PE ratio is 0.56 at 470 K, 0.63 at 500 K, and 0.73 at 530 K). As this reaction becomes irreversible at higher temperatures, the contribution of the initial O–H bond scission pathway to the overall rate of the EG decomposition increases (Figure 4A).

In the reaction pathway through the initial O–H bond scission, the reaction flux largely passes through a deep dehydrogenation of the α-carbon to $CHO\text{-}CH_2OH$ (glycolaldehyde) and $CO\text{-}CH_2OH$. In the reaction pathway through the initial C–H bond scission, β-H abstraction to CHOH-CHOH occurs first, followed by a C–H cleavage to COH-CHOH and a subsequent O–H cleavage to CO-CHOH. C–C cleavage is observed only after one side of the EG molecule is completely dehydrogenated (that is, only in $C_2H_xO_2$ intermediates with $x \leq 3$). Many C–C cleavage pathways are active at 500 K as shown by their relative contributions in Figure 3 ($CO\text{-}CH_2OH$: 28%, CO-CHOH: 24%, CO-CO: 22%, CO-CHO: 15%, and $CO\text{-}CH_2O$: 9%). The reforming mechanism shows a very high selectivity towards complete decomposition of ethylene glycol to carbon monoxide and hydrogen. In comparison, hydrogenation of CO to produce methanol is 2–5 orders of magnitude slower. Only at higher H_2 partial pressures (> 0.5 bar) did we observe more methanol than hydrogen production.

We used Campbell's degree of rate control[56] and degree of thermodynamic rate control[57-58] analyses to identify rate-controlling elementary steps and surface intermediates.

$$X_{RC,i} = \left[\frac{\partial \ln(r)}{\partial \left(\frac{-G_i^{0,TS}}{k_B T} \right)} \right]_{G_{j\neq i}^{0,TS},\, G_m^0} \quad ; \quad X_{TRC,n} = \left[\frac{\partial \ln(r)}{\partial \left(\frac{-G_n^{0}}{k_B T} \right)} \right]_{G_{m\neq n}^{0},\, G_i^{0,TS}} \qquad \ldots(12)$$

Here, $X_{RC,i}$ is the degree of rate control for elementary reaction i, $X_{TRC,n}$ is the degree of thermodynamic rate control for adsorbate n, r is the overall rate of reaction, $G_i^{0,TS}$ is the free energy of transitions state i, and G_n^0 is the free energy of adsorbate n. Results of these sensitivity analyses are summarized in Table 5. Along the dominant pathway for the EG decomposition, initial O–H bond scission and subsequent α-H abstraction to glycolaldehyde are the most kinetically relevant steps and collectively account for 75–85% of the overall degree of rate control.

Along the pathway through initial C–H scission, only the first dehydrogenation step shows an appreciable sensitivity coefficient. C–C cleaving reactions have no effect on the overall TOF. These observations are consistent with previous experimental and computational studies.[13-14] The degree of thermodynamic rate control is substantial only for H*, CO*, and COH*. All these species have a poisoning effect on the catalyst such that destabilizing their adsorption increases the overall reaction rate.

4.3. Aqueous-Phase Microkinetic Model

To account for an aqueous environment, free energies of solvation obtained from COSMO-RS calculations were used to reparametrize the microkinetic model. For an adsorption–desorption process[59]

$$\Delta G_L = \Delta G_G + G_{ads}(\text{solv}) - G_{Pt}(\text{solv}) \qquad \ldots(13)$$

where the subscripts G and L refer to the vapor/gas and liquid/aqueous phases, respectively. $G_{ads}(\text{solv})$ and $G_{Pt}(\text{solv})$ are the free energies of solvation for a Pt cluster with and without an adsorbate, respectively. Similarly, for a surface reaction

$$\Delta G_L = \Delta G_G + G_{FS}(\text{solv}) - G_{IS}(\text{solv}) \qquad \ldots(14)$$

$$\Delta G_L^{\ddagger} = \Delta G_G^{\ddagger} + G_{TS}(\text{solv}) - G_{IS}(\text{solv}) \qquad \ldots(15)$$

where the subscripts IS, FS, and TS stand for initial, final, and transition states, respectively.

Aqueous-phase reforming is simulated for the same set of process conditions as previously described for the vapor phase. The only difference is that the total pressure used to calculate free energies of solvation for adsorbed intermediates and transition states now additionally includes the saturation pressure of water at the simulation temperature, e.g., P_{H2O} = 26.4 bar at 500 K. In other words, the chemical potential of all fluid species in water is given by the partial pressure (fugacity) of the species in a vapor phase that is in equilibrium with the liquid phase, i.e., we assume gas-liquid equilibrium and no mass transfer limitations.

A crucial caveat of using an implicit solvation scheme to compute solvent effects is the uncertainty of the cavity radius of transition metal atoms. While for main group elements, implicit solvation models are reasonably accurate and predictive results can be obtained, cavity radii for transition metal elements wildly vary among various continuum solvation models. A list of cavity radii of transition metal atoms adopted for aqueous solvation calculations in different continuum solvation models is provided in the Supplementary Information. Specifically, the default cavity radius for Pt used in the PCM (Gaussian),[60] COSMO-RS (Turbomole/COSMOtherm),[44, 61-62] SM8 (universal solvation model),[63] and PBF (Jaguar)[64] solvation models are 2.33, 2.22, 1.74, and 1.38 Å, respectively. Our correspondence with Turbomole developers revealed that most of its default transition metal cavity radii are only "some guess" and the consequences of using different cavity radii might be significant. Figure S3 in the Supplementary Information reveals how the solvation energy for an adsorbed hydroxyl species changes from unfavorable to favorable solvation due to a change in cavity radius used in the above mentioned models. To understand how changing the cavity radius might play a role in the overall reaction mechanism, we performed our aqueous phase calculations at three different cavity radii for Pt: the default cavity radius included in the Turbomole program package, a 10% increased and a 10% decreased cavity radius. Unless stated otherwise, computational aqueous phase results are interpreted using the default cavity radius of Pt.

Figure 5 illustrates the effect of temperature on the coverage of the most abundant surface intermediates and overall TOFs. As in the vapor phase, CO* and H* are the dominant surface species. The CO* coverage however has increased (46–51%) and the H* coverage has significantly decreased (23–30%). No significant effect on surface coverage was found due to the introduction of a 10% incremental change in cavity radius of Pt. Adsorption energies reported in Table 3 show that adsorbed ethylene glycol, methanol, and CO are stabilized in water, whereas adsorbed hydrogen is destabilized. The larger equilibrium constant for EG adsorption results in an order of magnitude larger overall TOF (Figure 4B). Furthermore, the overall TOF changes by a factor of 0.7 to 1.7 owing to a change in the cavity radius of Pt by -10% and +10%, respectively, i.e., the overall TOF is relatively robust with respect to the change in cavity radius of Pt. This positive effect of an aqueous environment on the reaction rate is in agreement with experimental data. Shabaker et al.[21] reported a H_2 production TOF of 7.0 min^{-1} at 498 K for aqueous-phase reforming of ethylene glycol over 3.43% Pt/Al_2O_3. From the experimental data of Kandoi et al.,[10] the corresponding TOF at 498 K for vapor-phase reforming of ethylene glycol over 3.0% Pt/Al_2O_3 is estimated to be 2–3 min^{-1}.

The dependence of the overall TOF on the total system pressure and partial pressures of EG, CO, and H_2 in aqueous-phase reforming is shown in Figure 6 and summarized in Table 4. As before, the model-predicted ethylene glycol order (1.0) differs from the experimentally observed fractional order (0.3–0.5). The CO order is practically unchanged whereas the hydrogen order is now reduced to −0.47 (from −0.84 in vapor-phase reforming). As before the total system pressure has a strong inhibiting effect on the rate of EG decomposition. No significant effect on reaction orders was found as a result of altering the cavity radius for Pt atoms.

Figure 4A compares the relative contribution of initial C–H and O–H scission pathways to the total rate of ethylene glycol decomposition in both phases. In vapor-phase reforming, the relative contribution of the two pathways changes with temperature because the initial O–H cleavage reaction moves from partial equilibrium to irreversibility. Similar PE analysis in aqueous phase reveals that, because of a significantly lower H* coverage, this reaction is already far from equilibrium (computed PE ratio is 0.90 at 470 K, 0.95 at 500 K, and 0.97 at 530 K). As a result, the relative contribution of the two pathways is nearly constant at all temperatures. Decomposition through initial C–H bond scission becomes more important in aqueous phase which can be explained by a larger stabilization of this transition state compared to the O-H bond scission transition state in water. Table 2 shows that the free energy barrier for initial C–H bond cleavage is reduced from 0.83 eV to 0.75 eV in water. On the other hand, the free energy barrier for initial O–H bond cleavage is almost unaffected (0.71 eV and 0.70 eV in vapor and aqueous phases, respectively). As a result, the effect of water on the rate of initial C–H bond scission is considerably larger than that on initial O–H bond scission at all temperatures (Figure 4B). We note that it can be argued that O–H bond cleavage should be facilitated by inclusion of the coordinates of an explicit water molecule in the reaction coordinate of the O–H bond scission[65-67] — an effect not considered in this study that treats all solvent molecules implicitly. However, the pK_a value of ethylene glycol in water at 25 °C is 14.22 which corresponds to a free energy of dissociation of ethylene glycol (O–H bond cleavage and formation of a proton) in water of 0.84 eV. Considering that the free energy of activation for this process has to be larger than the free energy of reaction which is already larger than the free energy barrier computed by our implicit solvation model of 0.70 eV, direct O–H bond cleavage of ethylene glycol in liquid water is slower than the O–H bond cleavage on the metal surface. In other words, O–H bond scission has to involve direct participation of the metal and it is not evident to us that inclusion of explicit water coordinates in the reaction coordinate has to significantly facilitate O–H bond cleavage relative to C–H bond cleavage.

Figure 7 illustrates the fraction of the overall reaction flux passing through various pathways in aqueous-phase EG reforming at 500 K. Table 5 summarizes the results of a similar sensitivity analysis as described earlier. All surface intermediates and elementary reactions identified to be significant in this case are the same as previously determined from the analysis of the vapor-phase microkinetic model. Usage of different cavity radii for Pt (+/- 10%) does not change this observation. Noting that the relative fluxes through various elementary steps are also generally comparable, it can be concluded that the reaction chemistry of EG reforming is similar in both vapor and aqueous phases. This confirms the observation of Kandoi et al.[10] that similar values of kinetic parameters can be used to describe the vapor- and aqueous-phase reforming data suggesting a similar reaction mechanism in both phases.

4.4. Dispersion Effects

The microkinetic model presented in this work is generally able to reproduce experimentally observed kinetic trends. However, the disagreement between a model-predicted first order and previously reported fractional order with respect to ethylene glycol partial pressure requires further investigation. As Shabaker et al.[21] pointed out, a fractional order for ethylene glycol suggests that the coverage of EG-derived surface intermediates is significant under experimental conditions and there is competition for available free sites. Microkinetic simulations however predict that the coverage of all such intermediates is negligible. The origin of this discrepancy can be traced to a large positive free energy and a very small equilibrium constant for EG adsorption (Table 3). When adsorbed on a Pt(111) surface, saturated oxygenates like ethylene glycol and methanol do not form true chemical bonds to the metal. For such weakly chemisorbed systems, dispersion forces attain an increased relative importance.[68] These effects are not properly described by standard GGA functionals like PBE and the predicted adsorption energies are greatly underestimated.

To address this problem, we calculated the dispersion-corrected adsorption energy for ethylene glycol using the PBE-D3 method.[69] A separate Pt(111) slab was constructed for these calculations to account for a smaller equilibrium lattice constant (3.927 Å). Table 3 shows that the adsorption energy of ethylene glycol increases by 0.68 eV after dispersion effects are included. To maintain overall thermodynamic consistency, PBE-D3 calculations were also performed for all other gas-phase species (CO, H_2, and methanol).

Table 6 summarizes the predictions of vapor- and aqueous-phase microkinetic models when dispersion-corrected adsorption energies are used. The ethylene glycol order is still positive but now smaller than 1.0 in both phases. Negative reaction orders with respect to total pressure and partial pressures of carbon monoxide and hydrogen are correctly captured. Also, the overestimation of the apparent activation energy has also largely been corrected. CO* and H* are still the most dominant surface species and their coverages have increased from previous calculations reducing the availability of free sites. The coverage of ethylene glycol is on the order of 1% (an increase of 6–7 orders of magnitude). While the qualitative agreement with some experimental data is improved (due to a significant increase in ethylene glycol coverage but only a modest decrease in the availability of free sites), overall turnover frequencies are now over-predicted by 3–4 orders of magnitude. Thus, PBE-D3 likely overestimates adsorption energies and "true" adsorption energies are in between those computed by PBE and PBE-D3. Next, we observe that the effect of an aqueous environment on the mechanism of EG reforming is independent of whether dispersion effects are included or not and relative fluxes through various pathways remain largely unaffected and previous conclusions about the solvent effect on reforming rates remain applicable. Finally, the O–H and C–H bond scission steps remain the most rate controlling steps; although, CO and H_2 product desorption also become partially rate controlling particularly in an aqueous environment.

5. CONCLUSIONS

Mechanisms of Pt catalyzed vapor- and aqueous-phase ethylene glycol reforming for hydrogen production were systematically investigated using first-principles calculations. Detailed microkinetic models were developed to provide insights into the surface chemistry under realistic process conditions. The vapor-phase microkinetic model was parametrized using harmonic transition state theory and DFT-derived reaction energies and activation barriers. This model confirms that the dominant pathway for ethylene glycol decomposition is through initial O–H dehydrogenation, although the pathway through initial C–H cleavage remains kinetically relevant at all temperatures. A sensitivity analysis shows that only early dehydrogenation steps are rate determining. C–C bond cleavage occurs only after a significant dehydrogenation and almost exclusively in those intermediates where one of the cleavage products is CO. The reforming mechanism is highly selective toward complete decomposition to H_2 and CO and alternative pathways are not active except at higher hydrogen partial pressures (> 0.5 bar).

The aqueous-phase microkinetic model was parameterized using our continuum solvation approach (*iSMS*). This model predicts that an aqueous environment lowers the apparent activation energy and increases the rate of decomposition. While the pathway through initial O–H bond scission remains dominant in aqueous-phase reforming, disproportionate stabilization of the transition state for initial C–H bond breaking results in larger contribution of this pathway to the total rate of decomposition. The dominant surface intermediates and rate controlling steps remain unchanged from vapor-phase reforming and the relative reaction fluxes through various pathways are comparable, indicating that the reforming chemistry on platinum is similar in both phases. Finally, we investigated the effect of uncertainty in the cavity radius of Pt in the implicit solvation models on the overall TOF. No significant change was found on the coverages of the dominant surface species, apparent activation energy or reaction orders with respect to ethylene glycol, CO and H_2. Also, the uncertainty in the overall TOF in liquid water environments due to the uncertainty in the cavity radius of Pt is small relative to the increase in TOF due to solvation effects such that our conclusion that liquid water increases the reforming activity of alcohols over Pt(111) is robust with regards to the cavity radius of Pt.

ACKNOWLEDGEMENTS

This work was funded by the United States Department of Energy, Office of Basic Energy Sciences (No. DE-SC0007167). Computing resources provided by the Nanocenter at the University of South Carolina, National Energy Research Scientific Computing Center (NERSC), Environmental Molecular Science Laboratory (EMSL) computing resources provided by the Pacific Northwest National Laboratory (PNNL), and Extreme Science and Engineering Discovery Environment (XSEDE) computing resources provided by the Texas Advanced Computing Center (TACC) at the University of Texas at Austin (No. TG-CTS090100) are gratefully acknowledged.

ELECTRONIC SUPPLEMENTARY INFORMATION

Optimized structures for all surface intermediates and transition states, imaginary frequency and transition state bond lengths for all surface reactions, information about the data set used for fitting adsorbate–adsorbate lateral interaction parameters, a summary of the effects of incremental changes in cavity radii, and a summary of solvation effects on free energy changes of intermediates are provided.

REFERENCES

1. Huber, G. W.; Dumesic, J. A., An overview of aqueous-phase catalytic processes for production of hydrogen and alkanes in a biorefinery. *Catal Today* **2006,** *111* (1–2), 119–132.
2. Huber, G. W.; Iborra, S.; Corma, A., Synthesis of Transportation Fuels from Biomass: Chemistry, Catalysts, and Engineering. *Chem Rev* **2006,** *106* (9), 4044–4098.
3. Tanksale, A.; Beltramini, J. N.; Lu, G. M., A review of catalytic hydrogen production processes from biomass. *Renew Sust Energ Rev* **2010,** *14* (1), 166–182.
4. Cortright, R. D.; Davda, R. R.; Dumesic, J. A., Hydrogen from catalytic reforming of biomass-derived hydrocarbons in liquid water. *Nature* **2002,** *418* (6901), 964–967.
5. Davda, R. R.; Dumesic, J. A., Renewable hydrogen by aqueous-phase reforming of glucose. *Chem Commun* **2004,** (1), 36–37.
6. Kirilin, A. V.; Tokarev, A. V.; Kustov, L. M.; Salmi, T.; Mikkola, J. P.; Murzin, D. Y., Aqueous phase reforming of xylitol and sorbitol: Comparison and influence of substrate structure. *Appl Catal a-Gen* **2012,** *435*, 172–180.
7. Davda, R. R.; Shabaker, J. W.; Huber, G. W.; Cortright, R. D.; Dumesic, J. A., Aqueous-phase reforming of ethylene glycol on silica-supported metal catalysts. *Appl Catal B-Environ* **2003,** *43* (1), 13–26.
8. Davda, R. R.; Shabaker, J. W.; Huber, G. W.; Cortright, R. D.; Dumesic, J. A., A review of catalytic issues and process conditions for renewable hydrogen and alkanes by aqueous-phase reforming of oxygenated hydrocarbons over supported metal catalysts. *Appl Catal B-Environ* **2005,** *56* (1–2), 171–186.
9. Davda, R. R.; Dumesic, J. A., Catalytic Reforming of Oxygenated Hydrocarbons for Hydrogen with Low Levels of Carbon Monoxide. *Angew Chem Int Edit* **2003,** *42* (34), 4068–4071.
10. Kandoi, S.; Greeley, J.; Simonetti, D.; Shabaker, J.; Dumesic, J. A.; Mavrikakis, M., Reaction Kinetics of Ethylene Glycol Reforming over Platinum in the Vapor versus Aqueous Phases. *J Phys Chem C* **2011,** *115* (4), 961–971.
11. Shabaker, J. W.; Huber, G. W.; Davda, R. R.; Cortright, R. D.; Dumesic, J. A., Aqueous-phase reforming of ethylene glycol over supported platinum catalysts. *Catal Lett* **2003,** *88* (1–2), 1–8.
12. Huber, G. W.; Shabaker, J. W.; Evans, S. T.; Dumesic, J. A., Aqueous-phase reforming of ethylene glycol over supported Pt and Pd bimetallic catalysts. *Appl Catal B-Environ* **2006,** *62* (3–4), 226–235.
13. Salciccioli, M.; Yu, W. T.; Barteau, M. A.; Chen, J. G. G.; Vlachos, D. G., Differentiation of O-H and C-H Bond Scission Mechanisms of Ethylene Glycol on Pt and Ni/Pt Using Theory and Isotopic Labeling Experiments. *Journal of the American Chemical Society* **2011,** *133* (20), 7996–8004.
14. Salciccioli, M.; Vlachos, D. G., Kinetic Modeling of Pt Catalyzed and Computation-Driven Catalyst Discovery for Ethylene Glycol Decomposition. *Acs Catal* **2011,** *1* (10), 1246–1256.

15. Salciccioli, M.; Vlachos, D. G., Kinetic Modeling of Pt Catalyzed and Computation-Driven Catalyst Discovery for Ethylene Glycol Decomposition [ACS Catal. 1, 1246 (2011)]. *Acs Catal* **2012,** *2* (2), 306–306 Erratum.

16. Christiansen, M. A.; Vlachos, D. G., Microkinetic modeling of Pt-catalyzed ethylene glycol steam reforming. *Appl Catal a-Gen* **2012,** *431*, 18–24.

17. Norskov, J. K.; Bligaard, T.; Logadottir, A.; Bahn, S.; Hansen, L. B.; Bollinger, M.; Bengaard, H.; Hammer, B.; Sljivancanin, Z.; Mavrikakis, M.; Xu, Y.; Dahl, S.; Jacobsen, C. J. H., Universality in Heterogeneous Catalysis. *Journal of Catalysis* **2002,** *209* (2), 275–278.

18. Jones, G.; Bligaard, T.; Abild-Pedersen, F.; Norskov, J. K., Using scaling relations to understand trends in the catalytic activity of transition metals. *J Phys-Condens Mat* **2008,** *20* (6), 064239.

19. Alcala, R.; Mavrikakis, M.; Dumesic, J. A., DFT studies for cleavage of C-C and C-O bonds in surface species derived from ethanol on Pt(111). *Journal of Catalysis* **2003,** *218* (1), 178–190.

20. Greeley, J.; Mavrikakis, M., Competitive Paths for Methanol Decomposition on Pt(111). *Journal of the American Chemical Society* **2004,** *126* (12), 3910–3919.

21. Shabaker, J. W.; Davda, R. R.; Huber, G. W.; Cortright, R. D.; Dumesic, J. A., Aqueous-phase reforming of methanol and ethylene glycol over alumina-supported platinum catalysts. *Journal of Catalysis* **2003,** *215* (2), 344–352.

22. Hafner, J., Materials simulations using VASP — A quantum perspective to materials science. *Comput Phys Commun* **2007,** *177* (1–2), 6–13.

23. Kresse, G.; Joubert, D., From ultrasoft pseudopotentials to the projector augmented-wave method. *Phys Rev B* **1999,** *59* (3), 1758–1775.

24. Perdew, J. P.; Burke, K.; Ernzerhof, M., Generalized Gradient Approximation Made Simple. *Phys Rev Lett* **1996,** *77* (18), 3865–3868.

25. Perdew, J. P.; Burke, K.; Ernzerhof, M., Generalized gradient approximation made simple [Phys. Rev. Lett. 77, 3865 (1996)]. *Phys Rev Lett* **1997,** *78* (7), 1396–1396 Erratum.

26. Methfessel, M.; Paxton, A. T., High-precision sampling for Brillouin-zone integration in metals. *Phys Rev B* **1989,** *40* (6), 3616–3621.

27. Monkhorst, H. J.; Pack, J. D., Special points for Brillouin-zone integrations. *Phys Rev B* **1976,** *13* (12), 5188–5192.

28. Makov, G.; Payne, M. C., Periodic boundary conditions in *ab initio* calculations. *Phys Rev B* **1995,** *51* (7), 4014–4022.

29. Henkelman, G.; Uberuaga, B. P.; Jonsson, H., A climbing image nudged elastic band method for finding saddle points and minimum energy paths. *J Chem Phys* **2000,** *113* (22), 9901–9904.

30. Henkelman, G.; Jonsson, H., A dimer method for finding saddle points on high dimensional potential surfaces using only first derivatives. *J Chem Phys* **1999,** *111* (15), 7010–7022.

31. Heyden, A.; Bell, A. T.; Keil, F. J., Efficient methods for finding transition states in chemical reactions: Comparison of improved dimer method and partitioned rational function optimization method. *J Chem Phys* **2005,** *123* (22), 224101.

32. Faheem, M.; Suthirakun, S.; Heyden, A., New Implicit Solvation Scheme for Solid Surfaces. *J Phys Chem C* **2012,** *116* (42), 22458–22462.

33. Ribeiro, R. F.; Marenich, A. V.; Cramer, C. J.; Truhlar, D. G., Use of Solution-Phase Vibrational Frequencies in Continuum Models for the Free Energy of Solvation. *The Journal of Physical Chemistry B* **2011,** *115* (49), 14556-14562.

34. Ho, J.; Klamt, A.; Coote, M. L., Comment on the Correct Use of Continuum Solvent Models. *The Journal of Physical Chemistry A* **2010,** *114* (51), 13442-13444.

35. TURBOMOLE V6.4 2012, a development of University of Karlsruhe and Forschungszentrum Karlsruhe GmbH, 1989–2007, TURBOMOLE GmbH, since 2007.

36. Ahlrichs, R.; Bar, M.; Haser, M.; Horn, H.; Kolmel, C., Electronic Structure Calculations on Workstation Computers: The Program System TURBOMOLE. *Chem Phys Lett* **1989,** *162* (3), 165–169.

37. Schafer, A.; Huber, C.; Ahlrichs, R., Fully Optimized Contracted Gaussian Basis Sets of Triple-z Valence Quality for Atoms Li to Kr. *J Chem Phys* **1994,** *100* (8), 5829–5835.

38. Weigend, F.; Ahlrichs, R., Balanced basis sets of split valence, triple zeta valence and quadruple zeta valence quality for H to Rn: Design and assessment of accuracy. *Phys Chem Chem Phys* **2005,** *7* (18), 3297–3305.

39. Perdew, J. P., Density-functional approximation for the correlation energy of the inhomogeneous electron gas. *Phys Rev B* **1986,** *33* (12), 8822–8824.

40. Becke, A. D., Density-functional exchange-energy approximation with correct asymptotic behavior. *Phys Rev A* **1988,** *38* (6), 3098–3100.

41. Weigend, F., Accurate Coulomb-fitting basis sets for H to Rn. *Phys Chem Chem Phys* **2006,** *8* (9), 1057–1065.

42. Eichkorn, K.; Weigend, F.; Treutler, O.; Ahlrichs, R., Auxiliary basis sets for main row atoms and transition metals and their use to approximate Coulomb potentials. *Theor Chem Acc* **1997,** *97* (1–4), 119–124.

43. Klamt, A.; Schuurmann, G., COSMO: A New Approach to Dielectric Screening in Solvents with Explicit Expressions for the Screening Energy and its Gradient. *J Chem Soc Perk T 2* **1993,** (5), 799–805.

44. Schafer, A.; Klamt, A.; Sattel, D.; Lohrenz, J. C. W.; Eckert, F., COSMO Implementation in TURBOMOLE: Extension of an efficient quantum chemical code towards liquid systems. *Phys Chem Chem Phys* **2000,** *2* (10), 2187-2193.

45. Klamt, A., Conductor-Like Screening Model for Real Solvents – A New Approach to the Quantitative Calculation of Solvation Phenomena. *J Phys Chem-Us* **1995,** *99* (7), 2224–2235.

46. Klamt, A., *COSMO-RS: From Quantum Chemistry to Fluid Phase Thermodynamics and Drug Design*. Elsevier Science Ltd.: Amsterdam, The Netherlands, 2005.

47. Pechukas, P., Transition State Theory. *Annu Rev Phys Chem* **1981,** *32*, 159–177.

48. McQuarrie, D. A., *Statistical Mechanics*. University Science Books: Sausalito, CA, 2000.

49. Buzzi-Ferraris, G.; Manenti, F., BzzMath: Library Overview and Recent Advances in Numerical Methods. In *Computer Aided Chemical Engineering*, Bogle, I. D. L.; Fairweather, M., Eds. Elsevier: 2012; Vol. 30, pp 1312–1316.

50. Rubert-Nason, P.; Mavrikakis, M.; Maravelias, C. T.; Grabow, L. C.; Biegler, L. T., Advanced Solution Methods for Microkinetic Models of Catalytic Reactions: A Methanol Synthesis Case Study. *Aiche J* **2014,** *60* (4), 1336–1346.

51. Kandoi, S.; Greeley, J.; Sanchez-Castillo, M. A.; Evans, S. T.; Gokhale, A. A.; Dumesic, J. A.; Mavrikakis, M., Prediction of experimental methanol decomposition rates on platinum from first principles. *Top Catal* **2006,** *37* (1), 17–28.

52. Grabow, L. C.; Hvolbaek, B.; Norskov, J. K., Understanding Trends in Catalytic Activity: The Effect of Adsorbate-Adsorbate Interactions for CO Oxidation over Transition Metals. *Top Catal* **2010,** *53* (5–6), 298–310.

53. Salciccioli, M.; Chen, Y.; Vlachos, D. G., Density Functional Theory-Derived Group Additivity and Linear Scaling Methods for Prediction of Oxygenate Stability on Metal Catalysts: Adsorption of Open-Ring Alcohol and Polyol Dehydrogenation Intermediates on Pt-Based Metals. *J Phys Chem C* **2010,** *114* (47), 20155–20166.
54. Greeley, J.; Mavrikakis, M., A First-Principles Study of Methanol Decomposition on Pt(111). *Journal of the American Chemical Society* **2002,** *124* (24), 7193–7201.
55. Mhadeshwar, A. B.; Vlachos, D. G., Is the water-gas shift reaction on Pt simple? Computer-aided microkinetic model reduction, lumped rate expression, and rate-determining step. *Catal Today* **2005,** *105* (1), 162–172.
56. Campbell, C. T., Finding the rate-determining step in a mechanism – Comparing DeDonder relations with the "degree of rate control". *Journal of Catalysis* **2001,** *204* (2), 520–524.
57. Stegelmann, C.; Andreasen, A.; Campbell, C. T., Degree of Rate Control: How Much the Energies of Intermediates and Transition States Control Rates. *Journal of the American Chemical Society* **2009,** *131* (23), 8077–8082.
58. Stegelmann, C.; Andreasen, A.; Campbell, C. T., Degree of Rate Control: How Much the Energies of Intermediates and Transition States Control Rates [J. Am. Chem. Soc. 131, 8077 (2009)]. *Journal of the American Chemical Society* **2009,** *131* (37), 13563–13563 Erratum.
59. Behtash, S.; Lu, J.; Faheem, M.; Heyden, A., Solvent effects on the hydrodeoxygenation of propanoic acid over Pd(111) model surfaces. *Green Chemistry* **2014,** *16* (2), 605-616.
60. Frisch, M. J.; Trucks, G. W.; Schlegel, H. B.; Scuseria, G. E.; Robb, M. A.; Cheeseman, J. R.; Scalmani, G.; Barone, V.; Mennucci, B.; Petersson, G. A.; Nakatsuji, H.; Caricato, M.; Li, X.; Hratchian, H. P.; Izmaylov, A. F.; Bloino, J.; Zheng, G.; Sonnenberg, J. L.; Hada, M.; Ehara, M.; Toyota, K.; Fukuda, R.; Hasegawa, J.; Ishida, M.; Nakajima, T.; Honda, Y.; Kitao, O.; Nakai, H.; Vreven, T.; Montgomery Jr., J. A.; Peralta, J. E.; Ogliaro, F.; Bearpark, M. J.; Heyd, J.; Brothers, E. N.; Kudin, K. N.; Staroverov, V. N.; Kobayashi, R.; Normand, J.; Raghavachari, K.; Rendell, A. P.; Burant, J. C.; Iyengar, S. S.; Tomasi, J.; Cossi, M.; Rega, N.; Millam, N. J.; Klene, M.; Knox, J. E.; Cross, J. B.; Bakken, V.; Adamo, C.; Jaramillo, J.; Gomperts, R.; Stratmann, R. E.; Yazyev, O.; Austin, A. J.; Cammi, R.; Pomelli, C.; Ochterski, J. W.; Martin, R. L.; Morokuma, K.; Zakrzewski, V. G.; Voth, G. A.; Salvador, P.; Dannenberg, J. J.; Dapprich, S.; Daniels, A. D.; Farkas, Ö.; Foresman, J. B.; Ortiz, J. V.; Cioslowski, J.; Fox, D. J. *Gaussian 09*, Gaussian, Inc.: Wallingford, CT, USA, 2009.
61. Eckert, F.; Diedenhofen, M.; Klamt, A., Towards a first principles prediction of pK(a): COSMO-RS and the cluster-continuum approach. *Mol Phys* **2010,** *108* (3-4), 229-241.
62. Ahlrichs, R.; Bar, M.; Haser, M.; Horn, H.; Kolmel, C., Electronic-Structure Calculations on Workstation Computers - the Program System Turbomole. *Chem Phys Lett* **1989,** *162* (3), 165-169.
63. Marenich, A. V.; Olson, R. M.; Kelly, C. P.; Cramer, C. J.; Truhlar, D. G., Self-consistent reaction field model for aqueous and nonaqueous solutions based on accurate polarized partial charges. *J Chem Theory Comput* **2007,** *3* (6), 2011-2033.
64. Bochevarov, A. D.; Harder, E.; Hughes, T. F.; Greenwood, J. R.; Braden, D. A.; Philipp, D. M.; Rinaldo, D.; Halls, M. D.; Zhang, J.; Friesner, R. A., Jaguar: A high-performance quantum chemistry software program with strengths in life and materials sciences. *International Journal of Quantum Chemistry* **2013,** *113* (18), 2110-2142.
65. Yoon, Y.; Rousseau, R.; Weber, R. S.; Mei, D.; Lercher, J. A., First-principles study of phenol hydrogenation on Pt and Ni catalysts in aqueous phase. *Journal of the American Chemical Society* **2014,** *136* (29), 10287-10298.

66. Zope, B. N.; Hibbitts, D. D.; Neurock, M.; Davis, R. J., Reactivity of the Gold/Water Interface During Selective Oxidation Catalysis. *Science* **2010,** *330* (6000), 74-78.
67. Taylor, C. D.; Neurock, M., Theoretical insights into the structure and reactivity of the aqueous/metal interface. *Curr Opin Solid St M* **2005,** *9* (1-2), 49-65.
68. Klimes, J.; Michaelides, A., Perspective: Advances and challenges in treating van der Waals dispersion forces in density functional theory. *J Chem Phys* **2012,** *137* (12), 120901.
69. Grimme, S.; Antony, J.; Ehrlich, S.; Krieg, H., A consistent and accurate *ab initio* parametrization of density functional dispersion correction (DFT-D) for the 94 elements H-Pu. *J Chem Phys* **2010,** *132* (15), 154104.

Table 1. Lateral interaction parameters used in the microkinetic model.

Adsorbate pair	Lateral interaction (eV)
CO–CO	$1.0916(\theta_{CO} - 0.0296)$
H–H	$0.1414(\theta_{H} - 0.0227)$
CO–H	$\left(0.3185 + 0.3850\sqrt{\theta^*_{CO}\theta^*_{H}}\right)\theta^*_{H}$
X–X[a]	$1.0916\theta_{X}$
X–CO	$0.1086\theta_{CO}$
X–H	$0.0211\theta_{H}$

[a] X stands for all surface intermediates and transition states excluding CO and H.

Table 2. Energetics (eV) of surface reactions in the limit of zero coverage.

ID	Reaction	Zero-point Corrected		Vapor Phase (500 K)		Aqueous Phase (500 K)	
		$\Delta E^{\ddagger}$	ΔE_{rxn}	$\Delta G^{\ddagger}$	ΔG_{rxn}	$\Delta G^{\ddagger}$	ΔG_{rxn}
CC01	$CH_2OHCH_2OH{**} \rightarrow 2CH_2OH{*}$	2.07	–0.20	2.10	–0.20	1.98	–0.21
CC02	$CHOHCH_2OH{**} \rightarrow CHOH{*}+CH_2OH{*}$	1.34	–0.15	1.30	–0.18	1.24	–0.11
CC03	$CH_2OCH_2OH{**}+{*} \rightarrow CH_2O{**}+CH_2OH{*}$	1.39	–0.37	1.39	–0.43	1.44	–0.32
CC04	$COHCH_2OH{***} \rightarrow COH{*}+CH_2OH{*}+{*}$	1.42	–0.31	1.35	–0.38	1.34	–0.45
CC05	$CHOHCHOH{**} \rightarrow 2CHOH{*}$	1.02	–0.12	1.02	–0.09	1.06	+0.02
CC06	$CHOCH_2OH{***} \rightarrow CHO{*}+CH_2OH{*}+{*}$	1.23	–0.59	1.22	–0.74	1.21	–0.70
CC07	$CHOHCH_2O{**}+{*} \rightarrow CHOH{*}+CH_2O{**}$	0.80	–0.23	0.79	–0.28	0.76	–0.23
CC08	$CH_2OCH_2O{**}+2{*} \rightarrow 2CH_2O{**}$	0.61	–0.38	0.56	–0.45	0.39	–0.45
CC09	$COCH_2OH{**} \rightarrow CO{*}+CH_2OH{*}$	0.66	–0.92	0.63	–0.95	0.69	–0.89
CC10	$COHCHOH{**} \rightarrow COH{*}+CHOH{*}$	1.12	–0.23	1.09	–0.25	1.03	–0.27
CC11	$COHCH_2O{**}+{*} \rightarrow COH{*}+CH_2O{**}$	1.05	–0.35	1.03	–0.39	1.02	–0.42
CC12	$CHOCHOH{***} \rightarrow CHO{*}+CHOH{*}+{*}$	0.96	–0.51	0.90	–0.60	0.90	–0.56
CC13	$CHOCH_2O{***} \rightarrow CHO{*}+CH_2O{**}$	0.45	–0.72	0.46	–0.84	0.48	–0.78
CC14	$COCHOH{**} \rightarrow CO{*}+CHOH{*}$	0.41	–0.97	0.39	–0.97	0.46	–0.93
CC15	$COCH_2O{**}+{*} \rightarrow CO{*}+CH_2O{**}$	0.31	–0.82	0.32	–0.84	0.33	–0.85
CC16	$COHCOH{**} \rightarrow 2COH{*}$	1.08	–0.48	1.06	–0.48	1.01	–0.58
CC17	$COHCHO{**} \rightarrow COH{*}+CHO{*}$	0.95	–0.64	0.87	–0.72	0.79	–0.80
CC18	$CHOCHO{****} \rightarrow 2CHO{*}+2{*}$	0.91	–0.94	0.79	–1.14	0.78	–1.11
CC19	$COCOH{**} \rightarrow CO{*}+COH{*}$	0.64	–0.98	0.58	–1.00	0.58	–1.05
CC20	$COCHO{***} \rightarrow CO{*}+CHO{*}+{*}$	0.44	–1.30	0.38	–1.41	0.38	–1.39
CC21	$COCO{**} \rightarrow 2CO{*}$	0.02	–1.76	0.03	–1.76	0.05	–1.76

ID	Reaction	Zero-point Corrected		Vapor Phase (500 K)		Aqueous Phase (500 K)	
		$\Delta E^{\ddagger}$	ΔE_{rxn}	$\Delta G^{\ddagger}$	ΔG_{rxn}	$\Delta G^{\ddagger}$	ΔG_{rxn}
CH01	$CH_2OHCH_2OH** + * \rightarrow CHOHCH_2OH** + H*$	0.75	–0.48	0.83	–0.40	0.75	–0.39
CH02	$CHOHCH_2OH** + 2* \rightarrow COHCH_2OH*** + H*$	0.37	–0.41	0.38	–0.36	0.40	–0.29
CH03	$CHOHCH_2OH** + * \rightarrow CHOHCHOH** + H*$	0.35	–0.47	0.37	–0.46	0.34	–0.43
CH04	$CH_2OCH_2OH** + 2* \rightarrow CHOCH_2OH*** + H*$	0.11	–0.69	0.10	–0.64	0.07	–0.52
CH05	$CH_2OCH_2OH** + * \rightarrow CHOHCH_2O** + H*$	0.34	–0.57	0.33	–0.53	0.37	–0.39
CH06	$COHCH_2OH*** \rightarrow COHCHOH** + H*$	0.65	–0.51	0.64	–0.51	0.47	–0.47
CH07	$CHOHCHOH** + * \rightarrow COHCHOH** + H*$	0.54	–0.45	0.58	–0.41	0.61	–0.33
CH08	$CHOCH_2OH*** \rightarrow COCH_2OH** + H*$	0.37	–0.83	0.27	–0.90	0.31	–0.88
CH09	$CHOCH_2OH*** + * \rightarrow CHOCHOH*** + H*$	0.55	–0.52	0.46	–0.52	0.45	–0.43
CH10	$CHOHCH_2O** + * \rightarrow COHCH_2O** + H*$	0.56	–0.44	0.57	–0.45	0.55	–0.43
CH11	$CHOHCH_2O** + 2* \rightarrow CHOCHOH*** + H*$	0.05	–0.64	0.06	–0.63	0.05	–0.57
CH12	$CH_2OCH_2O** + 2* \rightarrow CHOCH_2O*** + H*$	0.19	–0.58	0.21	–0.57	0.19	–0.58
CH13	$COHCHOH** + * \rightarrow COHCOH** + H*$	0.71	–0.31	0.73	–0.33	0.67	–0.32
CH14	$COCH_2OH** + * \rightarrow COCHOH** + H*$	0.59	–0.38	0.61	–0.36	0.68	–0.26
CH15	$CHOCHOH*** \rightarrow COCHOH** + H*$	0.27	–0.70	0.21	–0.74	0.19	–0.71
CH16	$CHOCHOH*** \rightarrow COHCHO** + H*$	0.34	–0.44	0.33	–0.45	0.34	–0.39
CH17	$COHCH_2O** + * \rightarrow COHCHO** + H*$	0.14	–0.63	0.16	–0.63	0.18	–0.53
CH18	$CHOCH_2O*** \rightarrow COCH_2O** + H*$	0.14	–1.07	0.14	–1.10	0.17	–1.00
CH19	$CHOCH_2O*** + 2* \rightarrow CHOCHO**** + H*$	0.00	–0.70	0.04	–0.65	0.07	–0.57
CH20	$COCHOH** + * \rightarrow COCOH** + H*$	0.49	–0.56	0.50	–0.53	0.48	–0.50
CH21	$COHCHO** + * \rightarrow COCOH** + H*$	0.29	–0.81	0.30	–0.82	0.30	–0.82
CH22	$COCH_2O** + 2* \rightarrow COCHO*** + H*$	0.16	–0.43	0.18	–0.39	0.18	–0.36

ID	Reaction	Zero-point Corrected		Vapor Phase (500 K)		Aqueous Phase (500 K)	
		$\Delta E^{\ddagger}$	ΔE_{rxn}	$\Delta G^{\ddagger}$	ΔG_{rxn}	$\Delta G^{\ddagger}$	ΔG_{rxn}
CH23	CHOCHO**** → COCHO*** + H*	0.10	–0.80	0.08	–0.84	0.10	–0.79
CH24	COCHO*** → COCO** + H*	0.39	–0.71	0.36	–0.75	0.38	–0.70
CH25	CH_3OH*+* → CH_2OH*+H*	0.46	–0.43	0.48	–0.38	0.48	–0.31
CH26	CH_3O*+2* → CH_2O** + H*	0.08	–0.56	0.17	–0.50	0.17	–0.46
CH27	CH_2OH*+* → CHOH*+H*	0.37	–0.43	0.40	–0.38	0.41	–0.30
CH28	CH_2O** → CHO*+H*	0.34	–0.92	0.32	–0.96	0.33	–0.90
CH29	CHOH*+* → COH*+H*	0.34	–0.57	0.36	–0.57	0.32	–0.63
CH30	CHO*+* → CO*+H*	0.15	–1.16	0.21	–1.10	0.24	–1.07
OH01	CH_2OHCH_2OH** + * → CH_2OCH_2OH** + H*	0.63	+0.40	0.71	+0.48	0.70	+0.39
OH02	CH_2OCH_2OH** + * → CH_2OCH_2O** + H*	0.53	+0.23	0.58	+0.27	0.69	+0.41
OH03	$CHOHCH_2OH$** + 2* → $CHOCH_2OH$*** + H*	0.73	+0.18	0.75	+0.23	0.73	+0.26
OH04	$CHOHCH_2OH$** + * → $CHOHCH_2O$** + H*	0.89	+0.30	0.94	+0.35	0.97	+0.39
OH05	$CHOCH_2OH$***+* → $CHOCH_2O$*** + H*	0.75	+0.35	0.79	+0.34	0.80	+0.36
OH06	$CHOHCH_2O$** + 2* → $CHOCH_2O$*** + H*	0.95	+0.23	0.94	+0.23	0.95	+0.23
OH07	$COHCH_2OH$*** → $COCH_2OH$** + H*	0.20	–0.24	0.19	–0.30	0.12	–0.34
OH08	$COHCH_2OH$*** → $COHCH_2O$** + H*	0.52	+0.26	0.57	+0.25	0.58	+0.25
OH09	CHOHCHOH** + 2* → CHOCHOH*** + H*	0.60	+0.12	0.64	+0.17	0.67	+0.26
OH10	$COCH_2OH$** + * → $COCH_2O$** + H*	0.45	+0.11	0.52	+0.14	0.59	+0.25
OH11	$COHCH_2O$** + * → $COCH_2O$** + H*	0.11	–0.39	0.13	–0.42	0.19	–0.34
OH12	CHOCHOH***+2* → CHOCHO**** + H*	0.80	+0.17	0.80	+0.20	0.73	+0.22
OH13	COHCHOH** + * → COCHOH** + H*	0.41	–0.12	0.41	–0.16	0.41	–0.12
OH14	COHCHOH** + * → COHCHO** + H*	0.71	+0.14	0.72	+0.13	0.69	+0.20

ID	Reaction	Zero-point Corrected		Vapor Phase (500 K)		Aqueous Phase (500 K)	
		$\Delta E^{\ddagger}$	ΔE_{rxn}	$\Delta G^{\ddagger}$	ΔG_{rxn}	$\Delta G^{\ddagger}$	ΔG_{rxn}
OH15	$COCHOH^{**} + 2^{*} \rightarrow COCHO^{***} + H^{*}$	0.54	+0.07	0.62	+0.11	0.62	+0.14
OH16	$COHCHO^{**} + 2^{*} \rightarrow COCHO^{***} + H^{*}$	0.41	–0.19	0.44	–0.18	0.43	–0.18
OH17	$COHCOH^{**} + ^{*} \rightarrow COCOH^{**} + H^{*}$	0.47	–0.36	0.50	–0.35	0.49	–0.30
OH18	$COCOH^{**} + ^{*} \rightarrow COCO^{**} + H^{*}$	0.43	–0.08	0.45	–0.12	0.45	–0.06
OH19	$CH_3OH^{*} + ^{*} \rightarrow CH_3O^{*} + H^{*}$	0.65	+0.36	0.72	+0.36	0.75	+0.43
OH20	$CH_2OH^{*} + 2^{*} \rightarrow CH_2O^{**} + H^{*}$	0.61	+0.22	0.67	+0.25	0.69	+0.28
OH21	$CHOH^{*} + ^{*} \rightarrow CHO^{*} + H^{*}$	0.36	–0.27	0.35	–0.34	0.29	–0.33
OH22	$COH^{*} + ^{*} \rightarrow CO^{*} + H^{*}$	0.53	–0.86	0.55	–0.87	0.63	–0.77

Table 3. Energetics (eV) of adsorption reactions in the limit of zero coverage.

ID	Reaction	Zero-point Corrected ΔE_{rxn}		Vapor Phase ΔG_{rxn} (500 K)		Aqueous Phase ΔG_{rxn} (500 K)	
		PBE	PBE-D3	PBE	PBE-D3	PBE	PBE-D3
AD01	$CH_2OHCH_2OH + 2* \rightarrow CH_2OHCH_2OH**$	–0.46	–1.14	+0.58	–0.07	+0.52	–0.13
AD02	$CH_3OH + * \rightarrow CH_3OH*$	–0.27	–0.69	+0.65	+0.21	+0.58	+0.15
AD03	$CO + * \rightarrow CO*$	–1.79	–2.02	–0.98	–1.22	–1.00	–1.25
AD04	$H_2 + 2* \rightarrow 2H*$	–0.96	–1.06	–0.40	–0.49	–0.32	–0.41

Table 4. Kinetic properties at 500 K for vapor- and aqueous-phase reforming of ethylene glycol over Pt(111) for 1% conversion.

Property	Vapor Phase		Aqueous Phase	
	Model	Literature	Model	Literature
Apparent activation energy (eV)	1.52	0.83[a], 1.35[b], 0.59[c]	1.15	1.04[d]
Carbon monoxide order	–0.58	–0.4[a], –0.4[b], –0.54[c]	–0.61	
Hydrogen order	–0.84		–0.47	–0.5[d]
Ethylene glycol order	1.0	0.4[a], 0.05[b], 0.38[c]	1.0	0.3–0.5[d]
Total pressure order	–0.13	–0.10[a], –0.02[b], –0.26[c]	–1.89	–2.5[d]

[a] Experimental data[10]

[b] Model predictions[10]

[c] Model predictions[14]

[d] Experimental data[21]

Table 5. Sensitivity analysis for vapor- and aqueous-phase reforming of ethylene glycol over Pt (111).

	Vapor Phase			Aqueous Phase		
	425 K	500 K	525 K	425 K	500 K	525 K
Degree of rate control						
$CH_2OHCH_2OH** + * \rightarrow CHOHCH_2OH** + H*$	0.23	0.16	0.14	0.26	0.26	0.27
$CH_2OHCH_2OH** + * \rightarrow CH_2OCH_2OH** + H*$	0.19	0.35	0.51	0.66	0.69	0.70
$CH_2OCH_2OH** + 2* \rightarrow CHOCH_2OH*** + H*$	0.56	0.47	0.34	0.07	0.04	0.03
$CH_2OCH_2OH** + * \rightarrow CHOHCH_2O** + H*$	0.02	0.01	0.01			
Degree of thermodynamic rate control						
H*	–1.04	–0.83	–0.66	–0.68	–0.53	–0.44
CO*	–0.50	–0.44	–0.39	–0.44	–0.39	–0.36
COH*	–0.09	–0.02	–0.01	–0.21	–0.09	–0.03

Table 6. Summary of vapor- and aqueous-phase microkinetic model predictions with dispersion effects included.

Property	Vapor Phase	Aqueous Phase
Apparent activation energy (eV)	1.04	0.85
Carbon monoxide order	–0.45	–0.32
Hydrogen order	–1.01	–0.67
Ethylene glycol order	0.63	0.24
Total pressure order	–0.48	–0.34
Surface coverage at 500 K		
$CO*$	48%	57%
H*	43%	32%
*	7%	7%
CH_2OH-CH_2OH**	0.4%	0.9%

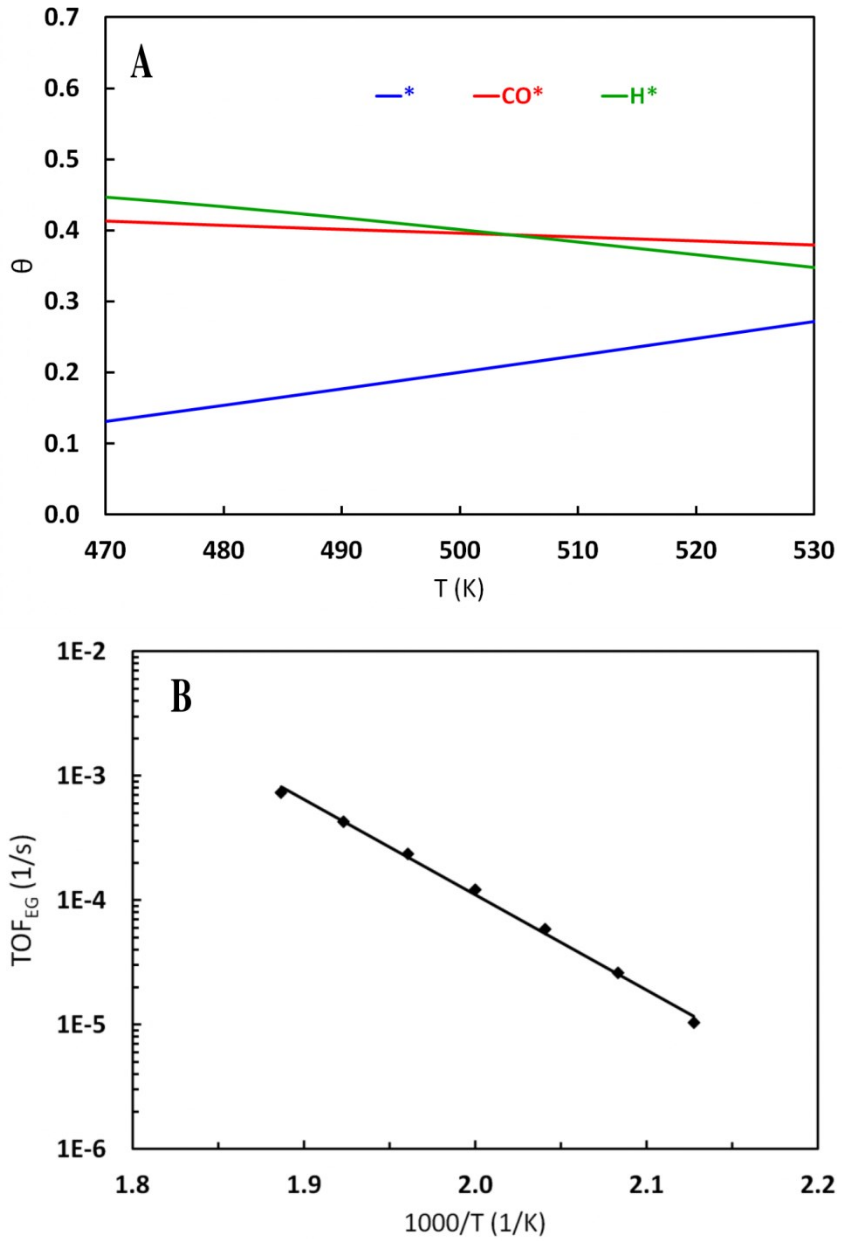

Figure 1. Effect of temperature on coverage of most abundant surface intermediates(A), and overall turnover frequency (B) in vapor-phase reforming of ethylene glycol over Pt(111).

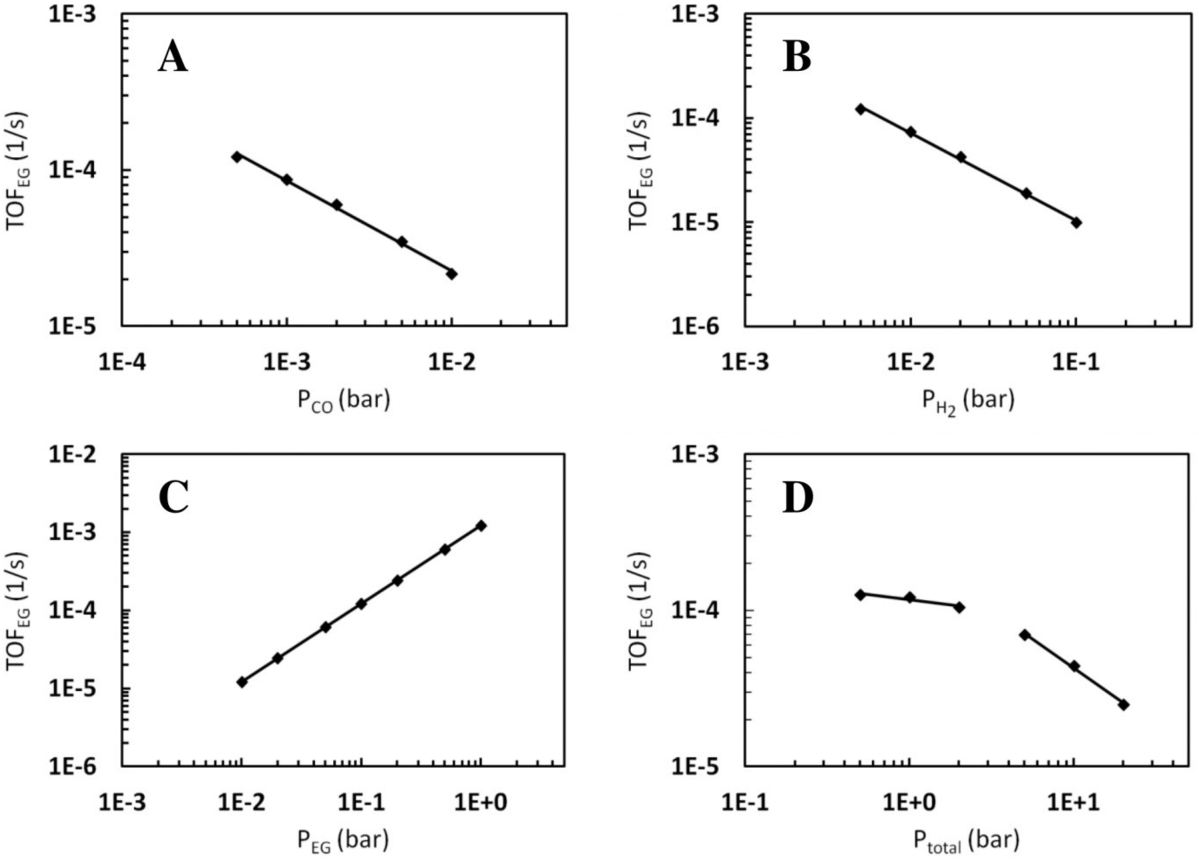

Figure 2. Effect of carbon monoxide partial pressure (A), hydrogen partial pressure (B), ethylene glycol partial pressure (C), and total pressure (D) on overall turnover frequency in vapor-phase reforming of ethylene glycol over Pt(111) at 500 K.

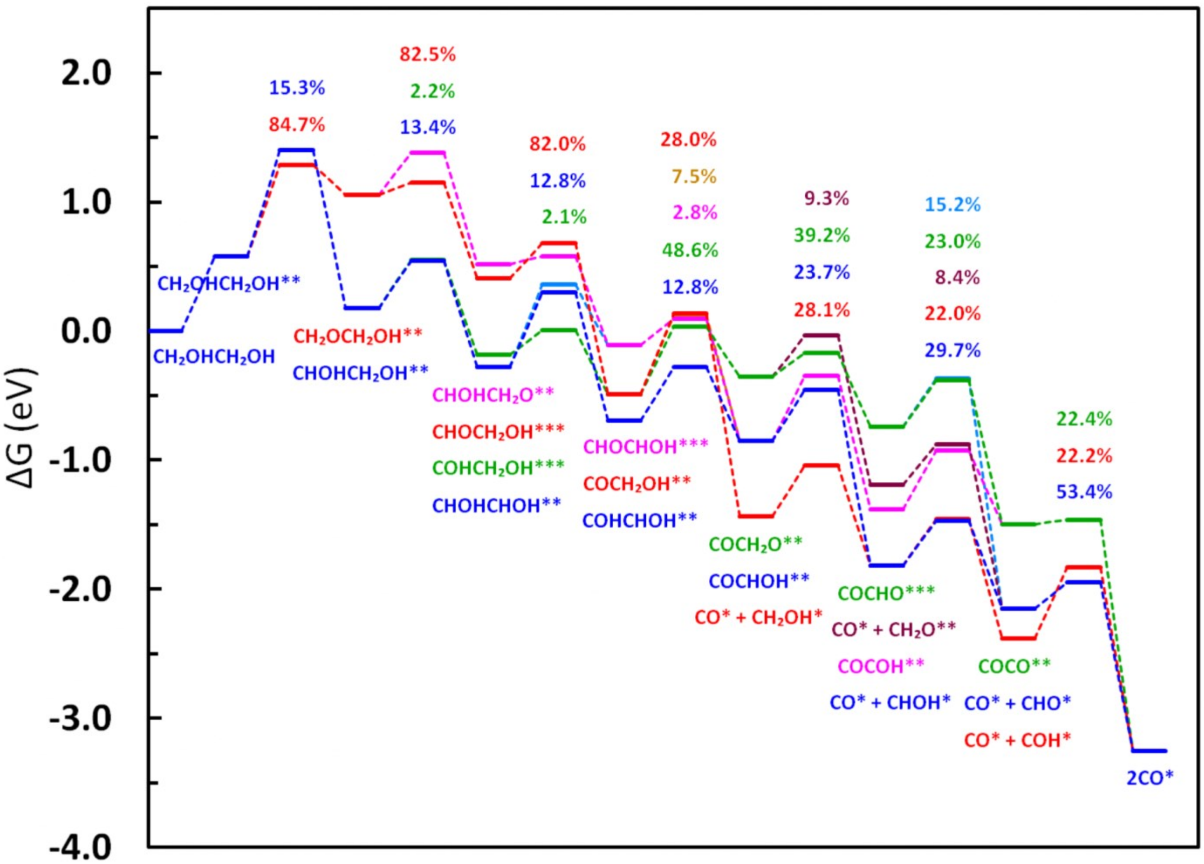

Figure 3. Free energy diagram at 500 K for vapor-phase reforming of ethylene glycol over Pt in the limit of zero coverage. Species labels show surface intermediates sorted (top to bottom) in order of increasing stability. Percent labels show fraction of the overall reaction flux passing through different pathways and are sorted (top to bottom) in order of increasing stability of respective transition states. Only those pathways are labeled that contribute more than 2% of the overall reaction flux. Excess hydrogen atoms are adsorbed on separate slabs and omitted from labels for simplicity.

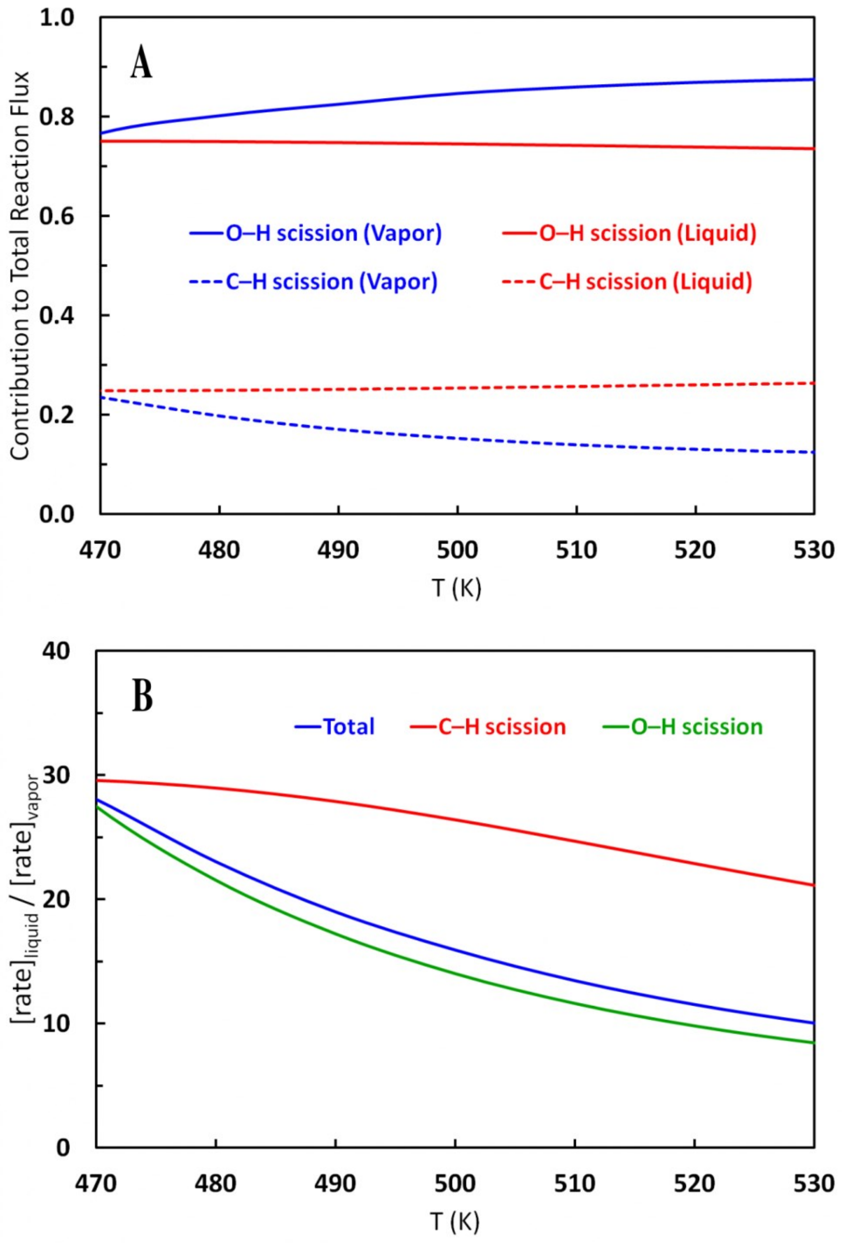

Figure 4. Comparison of vapor- and aqueous-phase reforming of ethylene glycol over Pt(111). (A) Contribution of initial C–H and O–H scission pathways to total rate of ethylene glycol decomposition. (B) Ratio of reaction rates in aqueous and vapor phases.

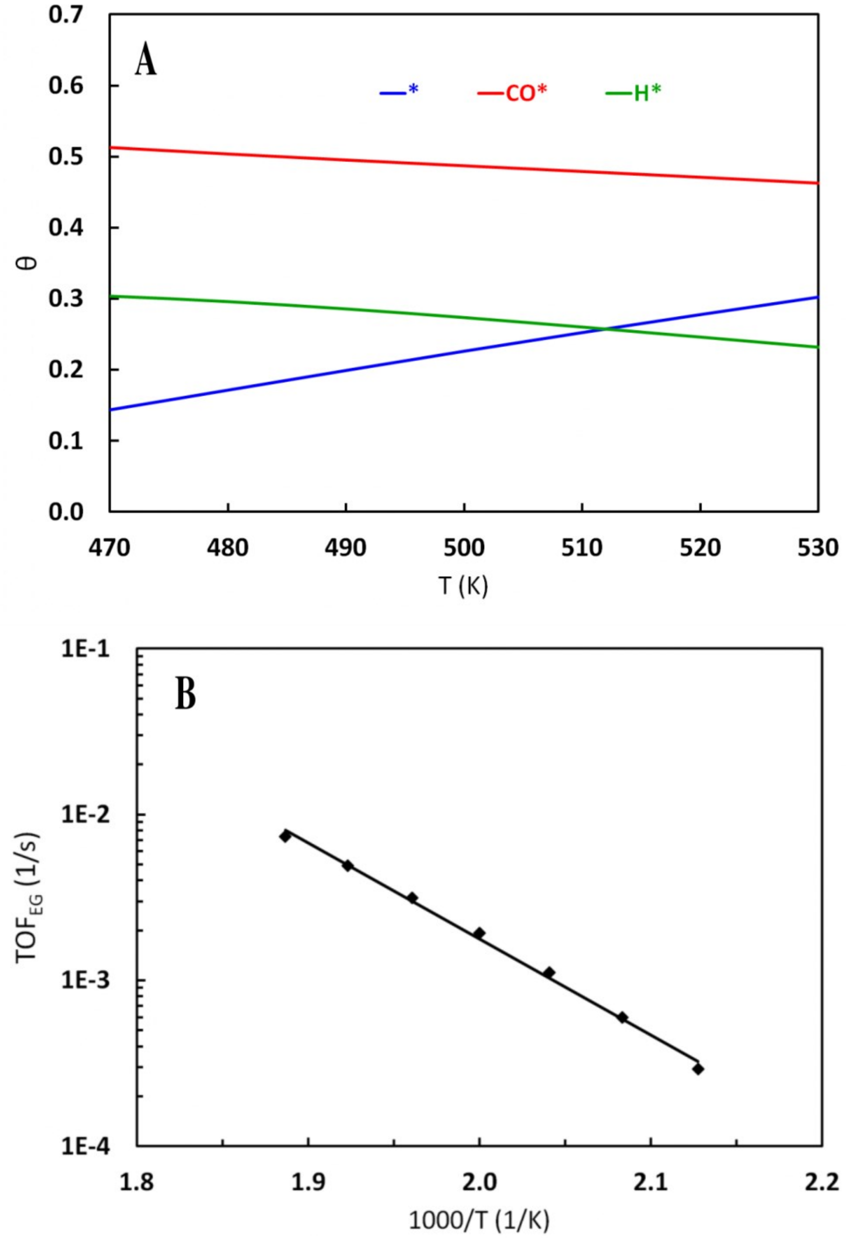

Figure 5. Effect of temperature on surface coverages of most abundant intermediates (A) and overall turnover frequency (B) in aqueous-phase reforming of ethylene glycol over Pt(111).

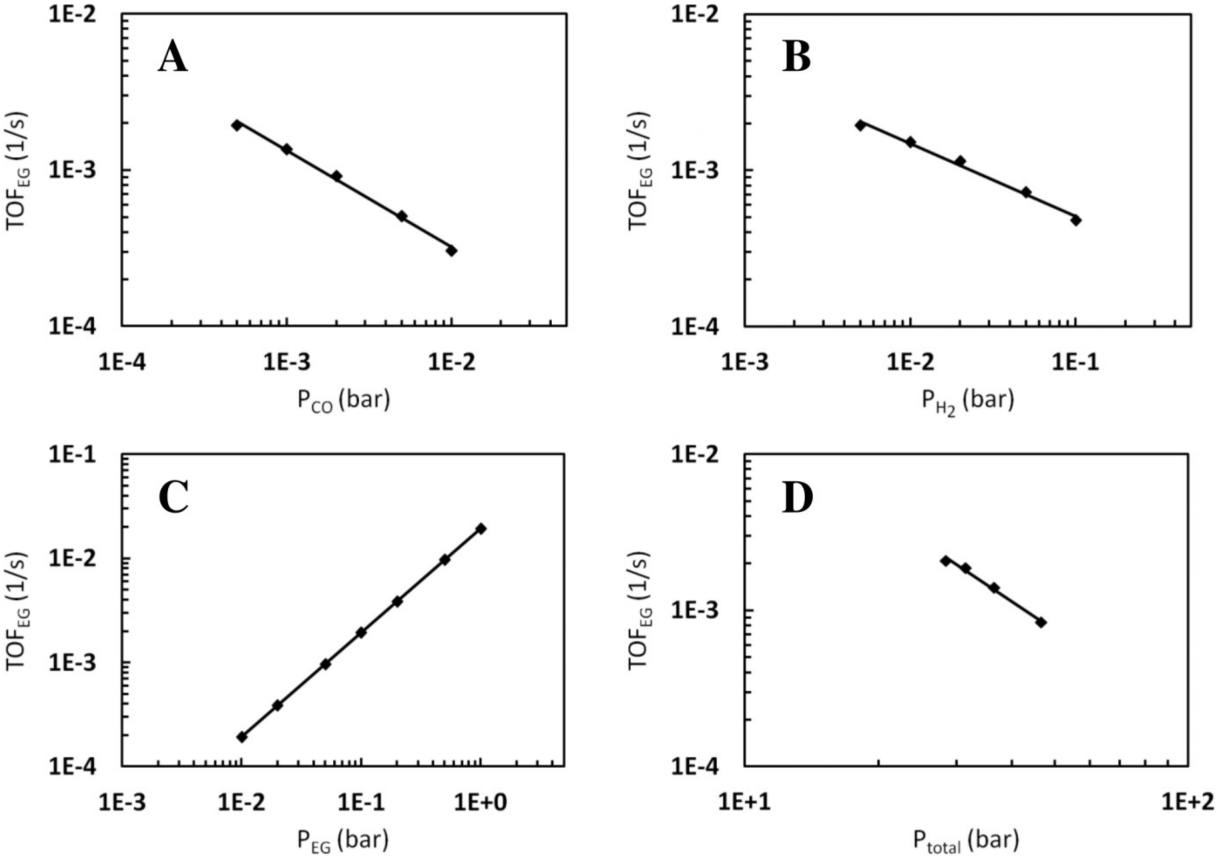

Figure 6. Effect of carbon monoxide partial pressure (A), hydrogen partial pressure (B), ethylene glycol partial pressure (C), and total pressure (D) on overall turnover frequency in aqueous-phase reforming of ethylene glycol over Pt(111) at 500 K.

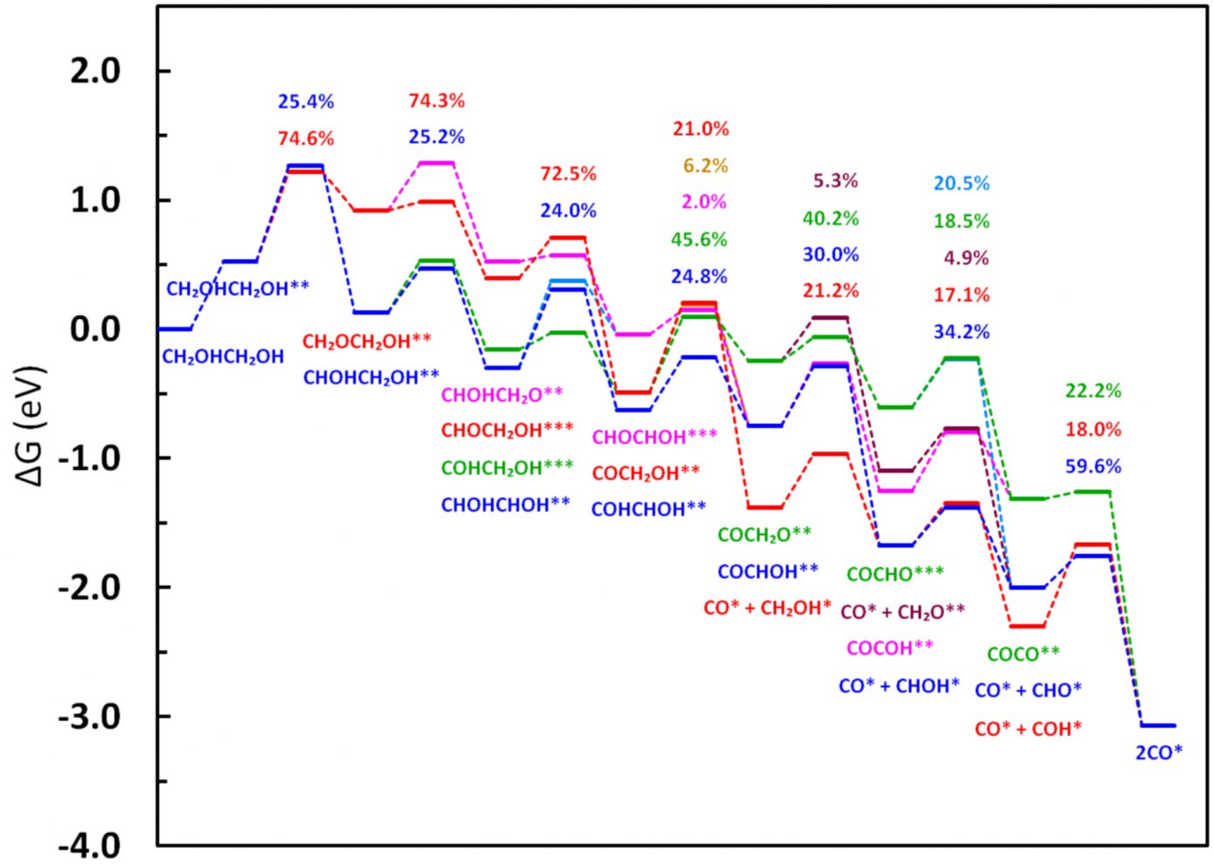

Figure 7. Free energy diagram at 500 K for aqueous-phase reforming of ethylene glycol over Pt in the limit of zero coverage. Species labels show surface intermediates sorted (top to bottom) in order of increasing stability. Percent labels above show fraction of the overall reaction flux passing through different pathways and are sorted (top to bottom) in order of increasing stability of respective transition states. Only those pathways are labeled that contribute more than 2% of the overall reaction flux. Excess hydrogen atoms are adsorbed on separate slabs and omitted from labels for simplicity.

TOC GRAPHIC

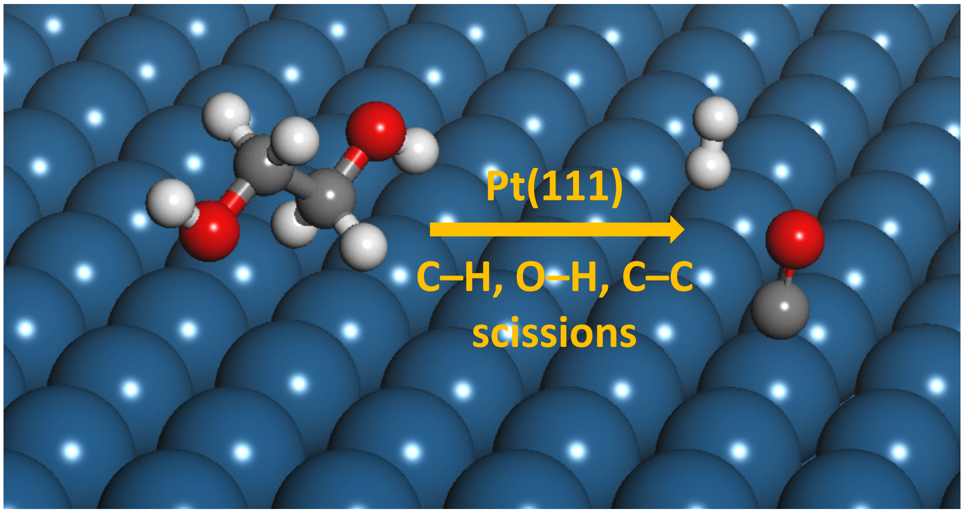

Reaction chemistry for vapor- and aqueous-phase reforming of ethylene glycol over Pt(111) is similar with early dehydrogenation steps being rate-controlling.